Modeling of Permeability and Formation Factor of Carbonate Digital Rocks: Dual-Pore-Network and Pore-Network-Continuum Models

Xingyuan Zhao[1] · Bowen Shi[1] · Xin Wang[1] · Jianlin Zhao[2] · Fei Jiang[3] · Chao-Zhong Qin[1]

Abstract

Many subsurface formations, such as soils, carbonate rocks, and mudstones, possess multi-scale pore structures that impose significant challenges to the pore-scale modeling of flow and transport processes. Despite the development of several models, there is a lack of comparative studies and quantitative analysis to evaluate their performance. In this work, we present two image-based hybrid models for predicting absolute permeability and electrical formation factor: a dual-pore-network model (DPNM) and a pore-network-continuum model (PNCM). We use several publicly available digital rock samples of Estaillades carbonate, one of which includes experimentally characterized sub-resolution regions (i.e., microporosity) represented by 3D maps of porosity and entry pressure. We perform comprehensive comparisons between the DPNM and PNCM, focusing on the strengths and limitations of the DPNM. Our results show that, assuming homogeneous microporosity, both the DPNM and PNCM accurately predict absolute permeability and formation factors. However, for realistic heterogeneous microporosity, the DPNM significantly underestimates absolute permeability by more than an order of magnitude, compared to the PNCM. We also explore two methods to improve the performance of our DPNM. Our findings will provide a foundation for the application of DPNMs to a wide range of geological and engineering systems.

Keywords Multiscale pore structures · Permeability and formation factor · Dual-pore-network model · Pore-network-continuum model · Microporosity · Digital rock physics

✉ Chao-Zhong Qin
chaozhong.qin@cqu.edu.cn

1　School of Resources and Safety Engineering, Chongqing University, Chongqing, People's Republic of China

2　College of Petroleum Engineering, China University of Petroleum, Beijing, China

3　Department of Mechanical Engineering, Graduate School of Sciences and Technology for Innovation, Yamaguchi University, Ube, Japan

1 Introduction

Flow and transport in porous media are critical to a wide range of subsurface and energy applications, including carbon dioxide sequestration (Alyafei and Blunt 2016; Gershenzon et al. 2016; Li et al. 2024), geothermal energy extraction (Jalilinasrabady et al. 2021), underground hydrogen storage (Heinemann et al. 2021), and electrochemical devices (Tjaden et al. 2017). The performance and efficiency of these applications are often governed by pore-scale fluid flow and transport processes within porous media. The advancement of imaging techniques (e.g., μCT) and high-performance computation has popularized image-based pore-scale modeling of porous media, being an important part of digital rock physics (DRP) (Bauer et al. 2012). However, many subsurface formations (e.g., carbonate rocks and mudstones) and electrochemical catalyst possess multiscale/hierarchical pore structures. Moreover, due to the trade-off between the image resolution and the field of view (FOV), there are abundant nanopores that cannot be resolved in a micrometer-scale image (Blunt et al. 2013). As a result, it remains a significant challenge to build efficient and accurate pore-scale models for multiscale porous media.

Traditionally, pore-scale numerical models are classified into direct numerical simulation (DNS) and pore-network models (PNMs). DNS (e.g., Navier–Stokes equation or lattice Boltzmann model) operates directly on segmented 3D images, predicting high-fidelity pore-scale flow dynamics (Carrillo et al. 2020; Carrillo and Bourg 2019; Soulaine 2024; Zhao et al. 2020, 2023). DNS is computationally intensive and faces the challenge in achieving the representative elementary volume (REV)-size modeling, particularly for complex multiphase flow dynamics (Ruspini et al. 2021). PNMs provide a computationally efficient alternative, leveraging state-of-the-art image-based pore-network extraction to incorporate essential features of pore structures. This enables PNMs to deliver quantitative predictions while maintaining computational feasibility (Dong and Blunt 2009; Gostick 2017; Liu et al. 2024). When addressing porous media with multiscale pore structures, it becomes essential to extend both DNS and PNMs to consider flow and transport in subresolution pores.

In the image-based modeling of multiscale porous media, resolved pores are usually referred to as resolved macropores, while sub-resolution pore regions are called microporosity (i.e., microporous regions) (Bultreys et al. 2015, 2016; Wang et al. 2022; Foroughi et al. 2024). For the sake of brevity, in what follows, the notation of macropores are referred to resolved macropores. Over recent years, three hybrid models tailored for multiscale pore structures have been developed, including microcontinuum models (MCMs) (Carrillo et al. 2020; Carrillo and Bourg 2019; Guo et al. 2018; Soulaine 2024), dual-pore-network models (DPNMs) (Bauer et al. 2012; Bultreys et al. 2015; Foroughi et al. 2024; Jiang et al. 2013; Koch et al. 2021; Mehmani et al. 2013; Mehmani and Prodanović 2014; Moslemipour and Sadeghnejad 2021; Wang et al. 2022) and pore-network-continuum models (PNCMs) (Shi et al. 2024; Zhang 2024). In MCMs, flow within macropores is modeled at the microscale by either the Navier–Stokes equation (Pinder and Gray 2008) or the lattice Boltzmann method (Zhao et al. 2016), whereas flow within microporosity is treated at the continuum scale using Darcy-type equations. This approach enables MCMs to achieve exceptional accuracy by explicitly modeling flow and transport in both macropores and microporosity (Carrillo et al. 2020). However, high computational demands associated with MCMs significantly limits their applicability to standard digital rock samples, which typically range from 1000^3 to 2000^3 voxels, similar to the constraints faced by DNS.

As an extension of classic PNMs, DPNMs incorporate an additional pore network to tackle flow and transport processes in microporosity. Two primary approaches exist for representing the pore network of microporosity. The first involves explicitly extracting a pore network from high-resolution images or numerically generating a network that represents microporosity's pore structures. However, this method is often impractical for most multiscale porous media due to the sheer abundance of nanopores in microporosity. The second approach treats microporosity on an average basis, allowing for the extraction of a watershed-based network of microporosity (Khan et al. 2019) or the proposal of microlinks (Bultreys et al. 2015; Foroughi et al. 2024) representing the microporous structure. When the latter approach is adopted in DPNMs, accurately characterizing the material properties of microporosity, such as porosity and permeability, becomes critical for quantitative predictions. Additionally, in some cases, microporosity may consist of multiple types of minerals, necessitating the extraction of more than one pore network for the microporosity. This scenario gives rise to "triple" or multiple pore-network models (Rabbani et al. 2020), which are variants of DPNMs.

To balance computational accuracy and efficiency, Zhang et al. (2024) proposed the framework of pore-network-continuum modeling for multiscale digital rocks. By imposing proper interface conditions, it couples the pore-network modeling of flow within macropores and the continuum-scale modeling of flow within microporosity as in MCMs. Most recently, Shi et al. (2024) developed a novel and robust algorithm for coarsening microporosity voxels of a multiscale digital rock, which can substantially reduce computational efforts of PNCMs. The efficiency and reliability of PNCMs with microporosity coarsening have been verified through numerical studies on incompressible single-phase flow, transient compressible single-phase flow, and transient solute transport (Shi et al. 2024).

The mini-review of the three hybrid models highlights the potential of DPNMs to simulate a few till tens of REVs, which will provide valuable insights into average-scale quantities and underlying physics. However, DPNMs simplify microporosity as a network of watersheds, relying on effective material properties such as mean porosities and pore sizes. This reliance may introduce a significant source of numerical errors, especially in highly heterogeneous microporosity. Currently, the performance of DPNMs in predicting flow and transport in multiscale digital rocks remains unclear. To address this gap, in this work, we develop an image-based DPNM and an image-based PNCM to predict two critical petrophysical parameters, i.e., absolute permeability and electrical formation factor. Comprehensive comparison studies are conducted to assess the applicability of DPNMs for modeling multiscale porous media. Additionally, we investigate the influence of image resolution on the prediction of absolute permeability and formation factor by using the DPNM, examining the trade-off between the FOV and the identification of macropores. This work will provide an essential step toward understanding the limitations and strengths of DPNMs for pore-scale modeling of flow and transport in multiscale porous media.

2 Materials and Methods

2.1 Digital Rocks of Estaillades Carbonate

We have selected three digital rocks of Estaillades carbonate from the Digital Rocks Portal (https://www.digitalrocksportal.org/), which are distinct in their spatial resolutions and pore structures. Estaillades limestone is composed of 99% calcite, which has multiscale

pore structures (Alyafei and Blunt 2016; Spurin et al. 2019a, b). Their μCT images show resolved macropores and sub-resolution microporosity with a bimodal distribution of pore sizes (Menke et al. 2022; Tanino and Blunt 2012). Table 1 lists the basic parameters of the three Estaillades digital rocks used in this work. Notice that they are from different core samples. For more details of the core samples, one can refer to their original research papers.

The total porosity of ES3.1 (ES denotes Estaillades and the spatial resolution is 3.1 μm) was determined by MIP (Mercury Intrusion Porosimetry). The experimental permeability was determined by averaging 15 measurements obtained with a Tiny Perm II portable probe permeameter on a 5^3 cm^3 test block (Bultreys et al. 2015). The total porosity of ES3.6 was determined by helium porosimeter, and none of permeability information was given (Spurin et al. 2019a, b). The microporosity of both ES3.1 and ES3.6 was not characterized. Therefore, we assume homogenous microporosity in the two digital rocks. With the help of in situ quasi-static drainage experiments and the differential imaging technique (Wang et al. 2022), the digital rock of ES6.5 has been well characterized including voxel-based porosity and entry pressure of microporosity. The experimental permeability of 202.4 ± 86.9 mD was determined by a minipermeameter.

3 Numerical Models

3.1 Dual-Pore-Network Model

In this section, we first describe how to construct the dual-pore-network of a multiscale digital rock. Then, our numerical model of single-phase incompressible fluid flow is presented in detail.

A greyscale μCT image is preprocessed with filtering and noise reduction techniques. Then, multithreshold segmentation is applied to identify solid, microporosity, and macropores. To be more precise, one can use the differential imaging technique to identify microporosity and its porosities, which needs a dry scan image and a high-salinity KI-saturated image (Lin et al. 2016). By using the open-source code, PoreSpy (Gostick 2017; Khan et al. 2019; Khan and Gostick 2024), we can generate individual watersheds of macropores and microporosity, and establish the connectivity map (i.e., network) of all the watersheds. Meanwhile, image-based analysis can give us the volume, surface area,

Table 1 The image and physical parameters of the three Estaillades digital rocks

Digital rock	Voxel size (μm)	Image size (voxels)	Total porosity (%)	Absolute permeability (mD)
				Experimental
ES3.1[a]	3.1	$2000 \times 2000 \times 1725$	25	260 ± 60
ES3.6[b]	3.6	$1000 \times 1000 \times 1000$	29	/
ES6.5[c]	6.5	$1316 \times 1316 \times 1087$	25	202.4 ± 86.9

[a]From Bultreys et al. (2015)

[b]From Spurin et al. (2019a, b)

[c]FromWang et al. (2022)

equivalent radius, and inscribed radius of each watershed, as well as the cross-sectional area, inscribed radius, equivalent radius, and perimeter of the 2D interface between two neighboring watersheds. Finally, the dual-pore-network of both macropores and microporosity is constructed including space coordinates, geometrical information, and the connectivity of all the watersheds. Notice that the definitions of pore bodies and pore throats specific to our DPNM will be given later on.

For the prediction of absolute permeability, we solve single-phase and incompressible fluid flow in a constructed dual-pore-network (e.g., Fig. 1d). The mass conservation equation is given as:

$$\sum_{j=1}^{N_i} Q_{ij} = \sum_{j=1}^{N_i} T_{ij}(p_i - p_j) = 0 \tag{1}$$

where the subscripts i and j are the pore body indices, ij is the pore throat index, N_i is the coordination number of pore body i, Q_{ij} (m^3/s) is the volumetric flux through the pore throat, T_{ij} (m^4/kg/s) is the total transmissibility between the two pore bodies, and p (Pa) is the fluid pressure. In our dual-pore-network model, there are three types of geometric connectivity between watersheds, namely, macropore-macropore, macropore-microporosity, and microporosity-microporosity. As illustrated in Fig. 2, each watershed of either macropore or microporosity is assumed to consist of two parts: pore body and half of the pore throat (notice that the so-called pore body or pore throat for a microporosity
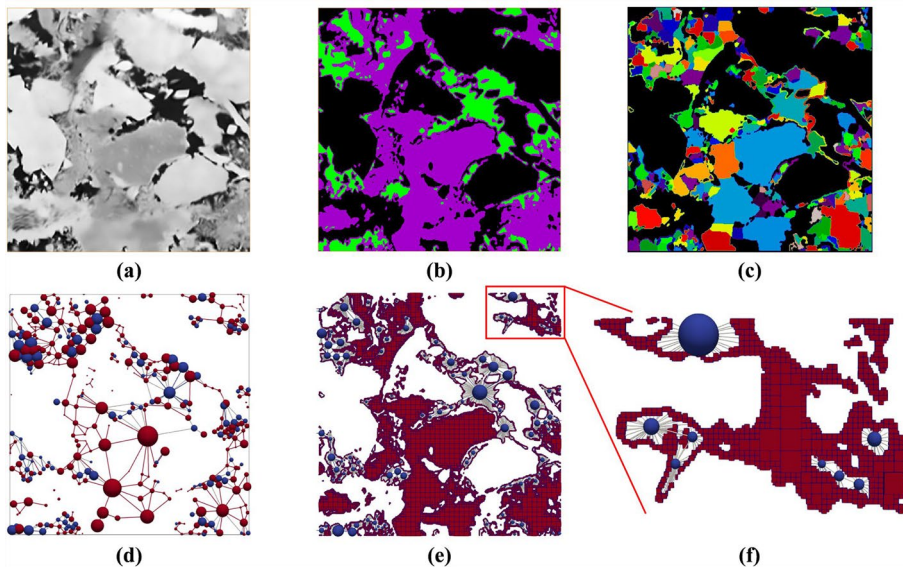
Fig. 1 Schematic of the image-based extraction of dual-pore-network and the generation of computational mesh for the PNCM. **a** A 400×400 grayscale slice of ES3.1. **b** The ternary image after threshold segmentation where the black represents solid, the purple represents sub-resolution microporosity, and the green represents resolved void spaces. **c** The individual watersheds of both void spaces (i.e., macropores) and microporosity. **d** The extracted dual-pore-network by PoreSpy, where the macropores and microporosity elements are in blue and red, respectively. **e** The computational mesh for the PNCM, where the original microporosity voxels are substantially coarsened to reduce computational efforts. **f** The zoom-in of the computational mesh.
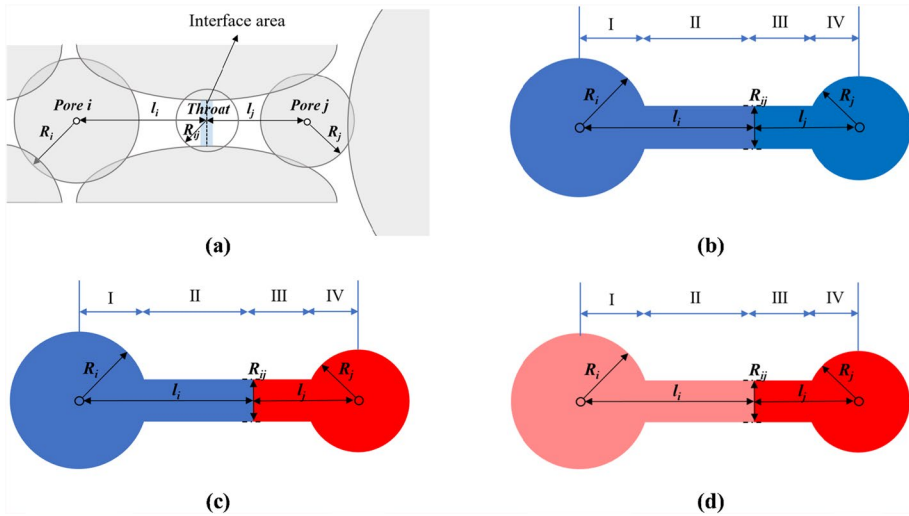
Fig. 2 2D schematic of the concept of idealized pore bodies and pore throats used in the DPNM. **a** Watersheds i and j, their equivalent radii, and their distances to the interface. Each watershed consists of two parts: pore body and half of the pore throat. The other half of the pore throat comes from the connected watershed. **b** Pore bodies and pore throat of the two macropore watersheds. **c** Pore bodies and pore throat of the macropore (blue) and microporosity (red) watersheds. **d** Pore bodies and pore throat of the two microporosity watersheds.

watershed is nominal, which is actually a sub-resolution porous region). The other half of the pore throat comes from the connected watershed of either macropore or microporosity. Notice that all the volume of a watershed is assigned to its pore body, and the pore throat is designed to account for transport resistance.

Based on the concept of idealized pore elements in Fig. 2, we can calculate the transmissibility in Eq. 1 as:

$$T_{ij} = \frac{a_i a_{ij}^{L} a_{ij}^{R} a_j}{a_i a_{ij}^{L} a_{ij}^{R} + a_i a_{ij}^{L} a_j + a_i a_{ij}^{R} a_j + a_{ij}^{L} a_{ij}^{R} a_j} \tag{2}$$

where a_i and a_j are the hydraulic conductance of pore body i and pore body j, respectively, a_{ij}^{R} is the hydraulic conductance of the right side of pore throat ij, being part of watershed j, and a_{ij}^{L} is the hydraulic conductance of the left side of pore throat ij, being part of watershed i. The four hydraulic conductance is listed in Table 2, in which k_i and k_j are the absolute permeability of microporosity watershed i and watershed j, respectively, R_i and R_j are the equivalent radii, R_{ij} is the equivalent radius of pore throat ij, l_i and l_j are the Euclidean distances between the centroids of pore body i and pore body j to the pore throat centroid, respectively, and μ is the dynamic viscosity. The left and right throat lengths ($l_i - R_i$, and $l_j - R_j$) may be negative due to the idealized pore elements, a minimum value of voxel size is used. In this work, we use the Katz–Thompson model (El-Dieb and Hooton 1994) to estimate microporosity permeability. For instance, for microporosity watershed i, its permeability is given as $k_i = \phi_i \bar{r}_i^2 / (32 \tau^2)$ where τ is the tortuosity of microporosity porous structures assumed to be constant (1.75) (Fu et al. 2021), ϕ_i is the mean porosity, and $\bar{r}_i$ is the mean pore size. We notice that, besides the Katz–Thompson model, some other

Table 2 Hydraulic conductance and electrical conductance in the calculation of transmissibility in Eqs. 1 and 6

Conductance	Macropores	Microporosity
Hydraulic conductance		
a_i	$\pi R_i^4/(8\mu R_i)$	$k_i \pi R_i^2/(\mu R_i)$
a_j	$\pi R_j^4/(8\mu R_j)$	$k_j \pi R_j^2/(\mu R_j)$
a_{ij}^L	$\pi R_{ij}^4/[8\mu(l_i - R_i)]$	$k_i \pi R_{ij}^2/[\mu(l_i - R_i)]$
a_{ij}^R	$\pi R_{ij}^4/[8\mu(l_j - R_j)]$	$k_j \pi R_{ij}^2/[\mu(l_j - R_j)]$
Electrical conductance		
b_i	$\sigma_w \pi R_i^2/R_i$	$\sigma_{w,i}^{\text{eff}} \pi R_i^2/R_i$
b_j	$\sigma_w \pi R_j^2/R_j$	$\sigma_{w,j}^{\text{eff}} \pi R_j^2/R_j$
b_{ij}^L	$\sigma_w \pi R_{ij}^2/(l_i - R_i)$	$\sigma_{w,i}^{\text{eff}} \pi R_{ij}^2/(l_i - R_i)$
b_{ij}^R	$\sigma_w \pi R_{ij}^2/(l_j - R_j)$	$\sigma_{w,j}^{\text{eff}} \pi R_{ij}^2/(l_j - R_j)$

empirical models may be used such as the Kozeny–Carmen model (Tiab and Donaldson 2016). The choice of a permeability model does not impact our main conclusions for the comparison between the DPNM and the PNCM.

Regarding the mean porosity of a microporosity watershed, ϕ_i, the calculation is as follows. In the CT images, voxel porosities are set to 0 and 1 for solid and resolved macropores, respectively. On the other hand, microporosity voxels have porosities between 0 and 1 (Lin et al. 2017, 2016; Wang et al. 2022), which can be determined by the following formula:

$$\varepsilon_k = \frac{\overline{I}^{\text{S}} - I_k^{\text{CT}}}{\overline{I}^{\text{S}} - \overline{I}^{\text{V}}} \tag{3}$$

where ε_k is the porosity of microporosity voxel k, I_k^{CT} is the CT gray value of microporosity voxel k, $\overline{I}^s$ is the average value of solid, and $\overline{I}^v$ is the average value of all macropores. Once the porosity of each microporosity voxel is known, the mean porosity of a microporosity watershed can be obtained by $\phi_i = \sum_{k=1}^{N_i} \varepsilon_k / N_i$ where N_i is the number of voxels in microporosity watershed i. Figure 3 shows the schematic of the porosity calculation for individual microporosity watersheds.

Regarding the mean pore size of a heterogeneous microporosity watershed, the calculation is as follows. Frist, the mean pore size of each microporosity voxel in the digital rock of
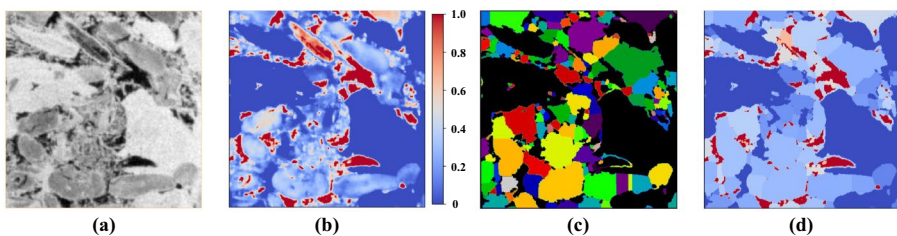
Fig. 3 Schematic of the porosity calculation of microporosity watersheds. **a** A 400×400 grayscale slice of ES6.5. **b** The porosity distribution where 0 for solid, 1 for resolved macropores, and 0–1 for microporosity. **c** The 185 microporosity watersheds. **d** The mean porosity distribution of watersheds.

ES6.5 is approximated by its invasion capillary pressure as $r_k = 2\sigma\cos\theta/P_{ct,k}$ where σ is the water–decane interfacial tension of 0.0483 N/m, θ is the contact angle of 0°, and $P_{ct,k}$ is the nonwetting-phase invasion capillary pressure of voxel k provided by Wang et al. (2022). It is worth noting that a mean pore size is usually larger than the pore size calculated by the invasion capillary pressure. Then, given the mean pore size of r_k, we can approximate the number of equivalent spherical pores in microporosity voxel k by $M_k = V_k\varepsilon_k/(4\pi r_k^3/3)$ where V_k is the voxel volume. Finally, the mean pore size of microporosity watershed i is calculated as:

$$\bar{r}_i = \left(\frac{3}{4\pi}\frac{\sum_{k=1}^{N_i} V_k\varepsilon_k}{\sum_{k=1}^{N_i} M_k}\right)^{1/3} \tag{4}$$

We impose the inlet and outlet pressure boundary conditions along the flow direction and no-flow boundary condition for the remainder. Then, Eq. 1 results in a set of linear algebraic equations for unknow pore body pressures, and the open-source Eigen solver is used in this work (Hakimov et al. 2022). Once the pressure field is known, we can obtain the inlet or outlet volumetric flow rate. Finally, the intrinsic permeability of a digital rock is obtained based on the Darcy equation as:

$$K = \frac{Q_{in}\mu L}{A\Delta p} \tag{5}$$

where K (m^2) is the intrinsic permeability, Q_{in} (m^3/s) is the inlet volumetric flow rate, L (m) is the length of the digital rock along the flow direction, A is the cross-sectional area of the digital rock, and Δp is the pressure drop along the flow direction.

Electrical formation factor is defined as the ratio of the electrical resistivity of a saturated porous medium to the resistivity of the fluid filling its pores. For formation factor calculations, we solve for the potential field in a dual-pore-network. The conservation equation of current is given as:

$$\sum_{j=1}^{N_i} I_{ij} = \sum_{j=1}^{N_i} T_{ij}^e(U_i - U_j) = 0 \tag{6}$$

where I_{ij} (A) is the current through pore throat ij, T_{ij}^e (S) is the total transmissibility between the two pore bodies, and U (V) is the potential. Similar to Eq. 2, we propose the following generalized formula for calculating the transmissibility in Eq. 6:

$$T_{ij}^e = \frac{b_i b_{ij}^L b_{ij}^R b_j}{b_i b_{ij}^L b_{ij}^R + b_i b_{ij}^L b_j + b_i b_{ij}^R b_j + b_{ij}^L b_{ij}^R b_j} \tag{7}$$

where b_i and b_j are the electrical conductance of pore body i and pore body j, respectively, b_{ij}^R is the electrical conductance of the right side of pore throat ij, being part of watershed j, and b_{ij}^L is the electrical conductance of the left side of pore throat ij, being part of watershed i. The four electrical conductance is given in Table 2, in which σ_w is the electrical conductivity of brine, and $\sigma_{w,i}^{eff}$ is the effective electrical conductivity of saturated microporosity watershed i given as $\sigma_{w,i}^{eff} = \sigma_w\phi_i^2/\tau$ (Tiab and Donaldson 2016).

The same numerical implement as single-phase flow is used for solving Eq. 6. Once the potential field is obtained, the effective electrical conductivity of a whole digital rock can be calculated by:

$$\sigma_{\text{network}} = \frac{I_{\text{in}}L}{A\Delta U} \tag{8}$$

where I_{in} is the total current at the inlet and ΔU is the potential difference across the domain. Finally, the formation factor of digital rock is calculated by $FF = \sigma_w/\sigma_{\text{network}}$.

3.2 Pore-Network-Continuum Model

In the PNCM, we use microporosity voxels as the computational grids instead of the network of microporosity watersheds used in the DPNM. Furthermore, we substantially coarsen the microporosity voxels to reduce computational costs as shown in Fig. 1f. In the mass conservation equation (Eq. 1), the calculation of T_{ij} is as follows. For a pair of macropore watersheds, we use Eq. 2. For a pair of microporosity grids, we have (Shi et al. 2024):

$$T_{ij} = \frac{a_i a_j}{a_i + a_j} \quad \text{with} \quad a_i = \frac{A_i k_i}{\mu d_i}\mathbf{n}_i \cdot \mathbf{f}_i, \quad a_j = \frac{A_j k_j}{\mu d_j}\mathbf{n}_j \cdot \mathbf{f}_j \tag{9}$$

where a_i is the transmissibility of grid i, a_j is the transmissibility of grid j, A_i is the interface area between the two grids which is equal to A_j, k_i is the intrinsic permeability of grid i (notice that in the dual-pore-network model, k_i is the intrinsic permeability of microporosity watershed i), d_i is the distance between the centroid of the interface and the centroid of grid i, $\mathbf{n}_i$ is the unit vector normal to the interface inside grid i and $\mathbf{f}_i$ is the unit vector along the direction of the line joining the centroid of grid i to the centroid of the interface. At the interfaces between macropores and microporosity grids, we have:

$$T_{ij} = \frac{a_i a_j}{a_i + a_j} \quad \text{with} \quad a_i = \frac{\pi R_i^4}{8\mu R_i}, \quad a_j = \frac{A_j k_j}{\mu d_j}\mathbf{n}_j \cdot \mathbf{f}_j \tag{10}$$

where a_i is the hydraulic conductance of pore body i and a_j is the transmissibility of microporosity grid j. In general, the resistance in macropores at the interfaces is slightly underestimated.

In formation factor (FF) calculations, for a pair of macropore watersheds, Eq. 7 is used to calculate the total transmissibility. For a pair of microporosity grids, the total transmissibility is calculated as:

$$T_{ij}^e = \frac{b_i b_j}{b_i + b_j} \quad \text{with} \quad b_i = \frac{A_i \sigma_{w,i}^{\text{eff}}}{d_i}\mathbf{n}_i \cdot \mathbf{f}_i b_j = \frac{A_j \sigma_{w,j}^{\text{eff}}}{d_j}\mathbf{n}_j \cdot \mathbf{f}_j \tag{11}$$

At the interfaces between macropores and microporosity grids, we have:

$$T_{ij}^e = \frac{b_i b_j}{b_i + b_j} \quad \text{with} \quad b_i = \frac{\pi R_i^2 \sigma_w}{R_i}, \quad b_j = \frac{A_j \sigma_{w,j}^{\text{eff}}}{d_j}\mathbf{n}_j \cdot \mathbf{f}_j \tag{12}$$

Finally, the Darcy equation and the equation for the effective electrical conductivity as in the dual-pore-network model (Eqs. 5, 8) are employed to compute the absolute permeability and formation factor. For the detail of the numerical implementation of the PNCM, one can refer to Shi et al. (2024 and Zhang (2024).

Table 3 Model verification assuming homogeneous microporosity permeability	Microporosity permeability	By DNS (mD)	By the reference model (mD)	Relative difference (%)
	10 mD	237	221	6.8
	100 mD	304	295	3
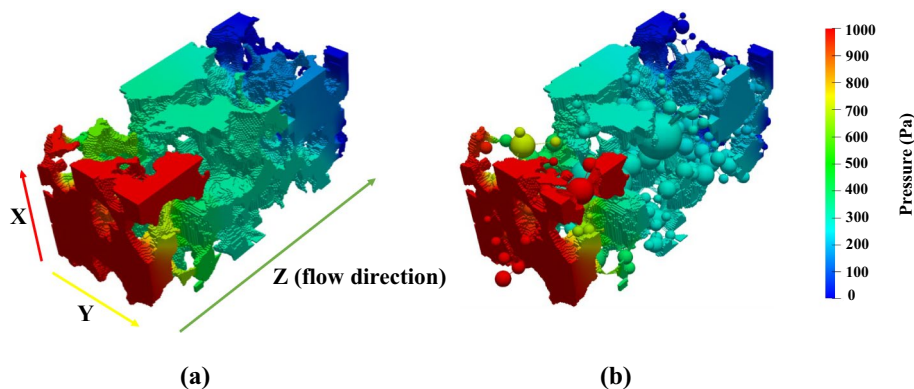
Fig. 4 **a** Pressure field predicted by the commercial solver Ansys fluent (DNS). **b** Pressure field predicted by the reference model.

4 Verification of the Reference Model

We use the MCM model (Guo et al. 2018; Soulaine 2024) by the finite-volume based commercial solver of Ansys Fluent and an in-house LBM solver to verify the PNCM without coarsening microporosity voxels, which is termed as the reference model in this work.

We first consider a multiscale digital rock with homogeneous microporosity permeability. A $100 \times 100 \times 200$ subvolume is extracted from a numerically synthesized multiscale digital rock of Berea sandstone (Shi et al. 2024). Its absolute permeability is simulated by both the DNS model in Ansys Fluent and the reference model. As listed in Table 3, compared to the DNS, the reference model can well predict the permeability at both low and high microporosity permeability, and the relative differences are small (e.g., 6.8% at low microporosity permeability). The simulated pressure distributions are shown in Fig. 4. Only minor discrepancy can be seen, due to the pore-network approximation of the macropores.

We further consider a multiscale digital rock with heterogeneous microporosity, i.e., ES6.5 in Table 1. As introduced above, the microporosity of ES6.5 has been experimentally characterized including voxel-based porosity and absolute permeability (the Katz-Thompson model). To reduce computational efforts, a 400^3 subvolume is extracted from the original image for the modeling. As listed in Table 4, the subvolume has about 3.7 million and 40.6 million voxels of macropores and microporosity, respectively. The absolute permeability is simulated by both an in-house LBM and the reference model. The Darcy term (i.e., the linear drag force) in microporosity is tackled by modifying the equilibrium distribution function and force term in the LBM (Guo and Zhao 2002). It is found that the reference model predicts the permeability of 174 mD, which matches the prediction

Table 4 The numbers of original voxels in the three simulated digital rocks and the numbers of pore bodies and computational grids in the two numerical models

Subvolume of digital rock	Pore regions	Original voxels	Volume fraction (%)	In the DPNM[a]	In the PNCM[b]
ES3.1	Macropores	6332318	9.9	3569	3569
	Microporosity	21562493	33.7	8375	3,929,815
ES3.6	Macropores	5040267	7.9	2172	2172
	Microporosity	32676964	51.1	13,228	4,494,989
ES6.5	Macropores	3694907	5.8	3827	3827
	Microporosity	40618405	63.5	7930	4,147,069

[a]The numbers of pore bodies (or watersheds) of macropores and microporosity in the DPNM.

[b]The numbers of pore bodies of macropores and coarsened grids of microporosity in the PNCM.

(186 mD) by the LBM with a relative error of 6.5%. To sum up, the reference model (i.e., the PNCM without coarsening microporosity voxels) has been well verified against the DNS in Ansys Fluent and the in-house LBM.

5 Results and Discussion

To reduce computational efforts, a 400^3 subvolume is extracted from each original image listed in Table 1, which may not reach the REV size. However, this should not impact the model comparison. Table 4 lists the information of pore elements and computational meshes used in the two models, i.e., the DPNM and the PNCM. It is seen that coarsening microporosity voxels substantially reduces the computational grids by over 85% in the PNCM. Then, Fig. 5 shows the grayscale images, the dual-pore-networks, and the computational meshes for the PNCM of the three digital rocks, namely, ES3.1, ES3.6, and ES6.5. Finally, in Sect. 4.1, both absolute permeability and formation factors predicted by the two models are compared; meanwhile, the values predicted by the reference model are used as the ground truth. In Sect. 4.2, we discuss the impact of image resolution on the prediction of absolute permeability by the DPNM.

6 Predictions of Permeability and Formation Factor

To compare the permeability predictions by the two models, we have conducted four case studies as outlined in Table 5. Four digital rocks including ES3.1, ES3.6, ES6.5-1, and ES6.5-2 are used, in which ES6.5-1 and ES6.5-2 have different mean pore sizes of microporosity. The microporosity of ES3.1, ES3.6, and ES6.5-1 is assumed to have uniform mean pore sizes (Ling et al. 2014; Tang et al. 2015), which are estimated by their MIP curves (see the detail in "Appendix 1"). The mean pore size of each microporosity voxel in ES6.5-2 is experimentally characterized in terms of its entry pressure, as described in Sect. 2.2.1. The image analysis shows that the macropores of the digital rocks are interconnected throughout the flow direction. ES3.1 has the best connectivity and the largest permeability of 117 mD predicted by the reference model. Table 5 lists the permeability values predicted by the DPNM and the PNCM. The permeability (174 mD) of ES6.5-2
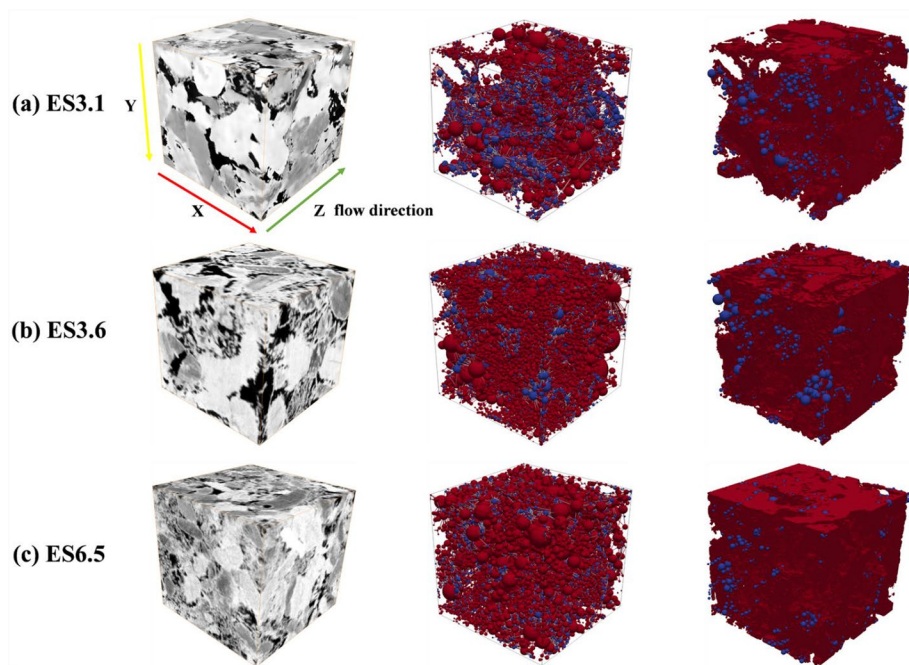
Fig. 5 Grayscale images (400^3), the dual-pore-networks, and the computational meshes for the PNCM of the three digital rocks of Estaillades carbonate, namely **a** ES3.1, **b** ES3.6, and **c** ES6.5. The blue is for macropores, while the red for microporosity.

Table 5 Comparisons of the permeability predicted by the DPNM, the PNCM, and the reference model

Digital rock	Mean pore size (μm)	By the DPNM (mD)	By the PNCM[b] (mD)	By the reference model[c] (mD)	Relative difference (DPNM, PNCM)
ES3.1	0.61	109	116	117	6.8%, 0.8%
ES3.6	0.74	34	37	37	8.1%, 0%
ES6.5-1	1.81	28	18	18	55%, 0%
ES6.5-2[a]	Estimated by entry pressure	12	128	174	93.1%, 26.4%

[a]Instead of a constant mean pore size assigned to all microporosity, the mean pore size of each microporosity voxel is experimentally characterized (Wang et al. 2022).

[b]The PNCM is the practical pore-network-continuum model with coarsening microporosity voxels.

[c]The reference model is the pore-network-continuum model without coarsening microporosity voxels.

predicted by the reference model matches the experimental value of 202 mD in Table 1. For the first three digital rocks with microporosity of uniform mean pore sizes, the PNCM predicts the same permeability values as those by the reference model, although over 85% of computational grids are reduced by coarsening microporosity voxels. Moreover, it is found that the DPNM can also well predict permeability with slight discrepancies. However, for ES6.5-2, the PNCM underestimates permeability by approximately 26%, while

the DPNM significantly underestimates permeability by over an order of magnitude (about 92%). Moreover, the predicted value of 12 mD by the DPNM is close to the value of 9.54 mD predicted by the porosity-based sub-rock typing DPNM model in Wang et al. (2022).

It is crucial to investigate the underlying reasons for the poor performance of the DPNM in predicting permeability in the presence of pronounced heterogeneity of mean pore sizes in microporosity (ES6.5-2 in this work). Firstly, we explain why the approximation of porosities of coarsened grids in the PNCM and watersheds in the DPNM does not significantly impact their permeability predictions. Figure 6a shows the cumulative distributions of the porosities of the original microporosity voxels, the microporosity watersheds in the DPNM, and the coarsened microporosity grids in the PNCM for ES6.5-1. As expected, due to the local averaging of voxel porosities, the distribution curve for the coarsened microporosity grids becomes flatter, compared to the curve for the original microporosity voxels. Interestingly, the distribution curve for the microporosity watersheds nearly coincides with the curve for the original microporosity voxels, except at low porosities. This is because the porosities of microporosity voxels in each watershed are relatively homogenous (refer to Fig. 3b, d). Correspondingly, the similar trends of the cumulative distributions of the permeability of the original microporosity voxels, the microporosity watersheds in the DPNM, and the coarsened microporosity grids in the PNCM are shown in Fig. 6b. Moreover, due to the assumption of uniform mean pore sizes, microporosity permeability spans only one to two orders of magnitude.

Secondly, we hypothesize that the discrepancies in permeability prediction are mainly due to the approximation (refer to Eq. 4) of mean pores sizes of coarsened grids in the PNCM and microporosity watersheds in the DPNM. Fig. 7a shows the cumulative distributions of the mean pore sizes of the original microporosity voxels, the watersheds in the DPNM, and the coarsened microporosity grids in the PNCM. It is seen that the distribution curve for the coarsened microporosity grids slightly deviates from the reference curve for the original microporosity voxels, whereas the curve for the watersheds significantly deviates from the reference curve with majority of mean pore radii smaller than 2 μm. Consequently, microporosity permeability in the DPNM is dramatically underestimated as shown in Fig. 7b. Given the fact that the macropores of ES6.5-2 are not interconnected throughout
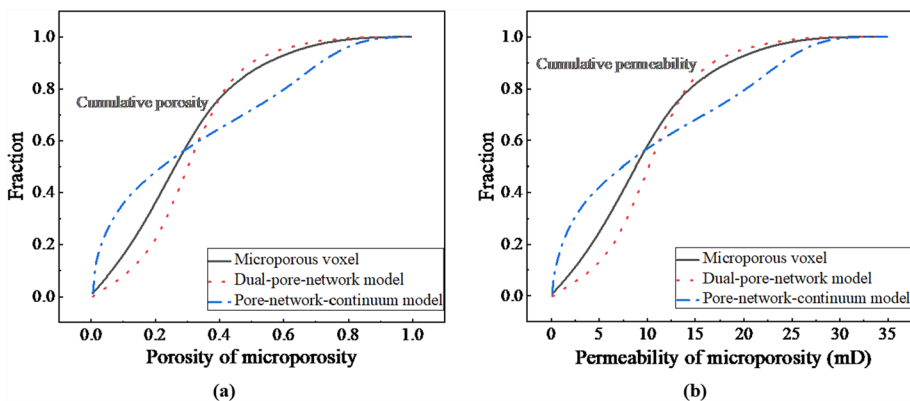
Fig. 6 **a** Cumulative distributions of the porosities and **b** the cumulative distributions of the permeability of the original microporosity voxels, the microporosity watersheds in the DPNM, and the coarsened microporosity grids in the PNCM for ES6.5-1.
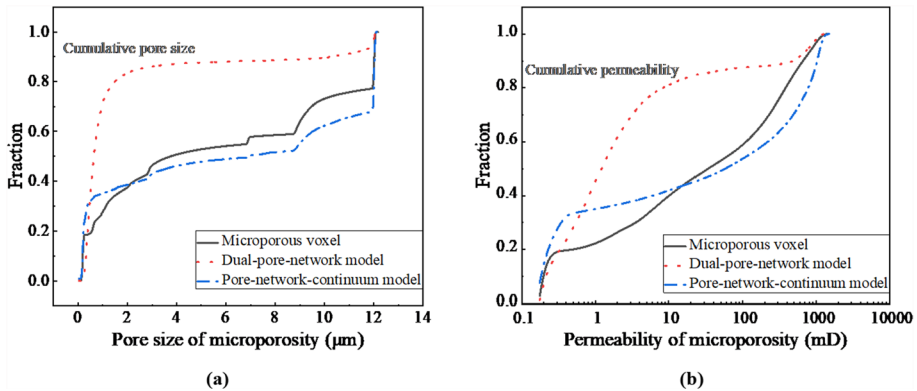
Fig. 7 **a** Cumulative distributions of the mean pore sizes and **b** the cumulative distributions of the permeability of the original microporosity voxels, the watersheds in the DPNM, and the coarsened microporosity grids in the PNCM for ES6.5-2. The mean pore size of each microporosity grid or watershed is calculated by Eq. 4.

the domain (Wang et al. 2022), this can well explain why the DPNM underestimates the permeability of ES6.5-2 by over an order of magnitude. Moreover, it is seen that the heterogeneous mean pore sizes of microporosity together with the heterogeneous mean porosities cause microporosity permeability to span 3–4 orders of magnitude.

Besides the modeling of permeability, we simulate formation factors of the three digital rocks. Notice that electrical resistance depends on the porosities of microporosity, but not the mean pore sizes of microporosity (refer to Table 2). Therefore, we do not distinguish ES6.5-1 and ES6.5-2 in the modeling of formation factor. Table 6 lists the formation factors predicted by the DPNM, the PNCM, and the reference model. In consistence with the findings in predicting permeability of the three digital rocks (i.e., ES3.1, ES3.6, and ES6.5-1), both the DPNM and PNCM can well reproduce the formation factors given by the reference model.

Thus far, we have demonstrated that permeability prediction by the DPNM is poor when dealing with heterogeneous mean pore sizes in microporosity. To address this issue, we propose two approaches to improve the performance of the DPNM. Assuming the spatial distribution of the mean pore sizes of microporosity voxels is known, instead of Eq. 4, we may calculate the mean pore size of each microporosity watershed by the arithmetic average of mean pore sizes of the voxels included in a watershed:

$$\bar{r}_j = \frac{\sum_{k=1}^{N_i} \sum r}{N_i} \tag{13}$$

Table 6 Comparisons of the formation factor predicted by the DPNM, the PNCM, and the reference model

Digital rock	By the DPNM (−)	By the PNCM (−)	By the reference model (−)
ES3.1	17.24	19.61	19.23
ES3.6	23.81	23.81	23.26
ES6.5	18.52	20.41	19.23

Interestingly, the predicted permeability of 205 mD slightly exceeds the value of 174 mD by the reference model. This can be explained by the distributions of the mean pore sizes and permeability of microporosity watersheds. As shown in Fig. 8a, the cumulative distribution of mean pore sizes in the DPNM shifts to the right, indicating an over-estimation of mean pore sizes compared to those of microporosity voxels in the reference model. Consequently, this leads to an overestimation of microporosity permeability as shown in Fig. 8b.

The second approach is based on the entry pressure-based sub-rock typing proposed by Wang et al. (2022). Five sub-rock types were obtained corresponding to the five entry pressure values of 14, 80, 180, 220, and 400 kPa. Figure 9 shows the five zones of microporosity in a cross section of ES6.5. Based on the Young-Laplace equation, the corresponding pore radii are 0.24, 0.44, 0.54, 1.21, and 6.9 μm. By using the PoreSpy, we can extract five individual pore networks of the five sub-rock types of microporosity, and then merge them together forming the pore network of microporosity. We further conduct image-based merging of the pore network of microporosity and the pore network of macropores forming the dual-pore-network. With the extracted dual-pore-network and the distribution of five mean pore sizes of microporosity, our DPNM predicts the permeability of 112 mD for ES6.5-2. The prediction improvement is considerable, because the used sub-rock typing can avoid the approximation of mean pore sizes of microporosity watersheds in the DPNM. Figure 10a shows the cumulative distributions of the mean pore sizes of the original microporosity voxels and the watersheds in the DPNM. As stated above, the continuous distribution of the mean pore sizes of the original microporosity voxels is approximated by the five discrete mean pore sizes. Together with the mean porosities of microporosity (Fig. 6a), the five discrete mean pore sizes give rise to the cumulative distribution of the permeability of the microporosity watersheds in the DPNM as shown in Fig. 10b, which matches the cumulative distribution of the original microporosity voxels much better than that in Fig. 7b.

When the same digital rock (Table 1) and the same sub-rock typing as in Wang et al. (2022) are used, by the DPNM we predicted a different permeability value of 155 mD, versus 69.5 mD in Wang et al. (2022). This is because we used the Young–Laplace equation
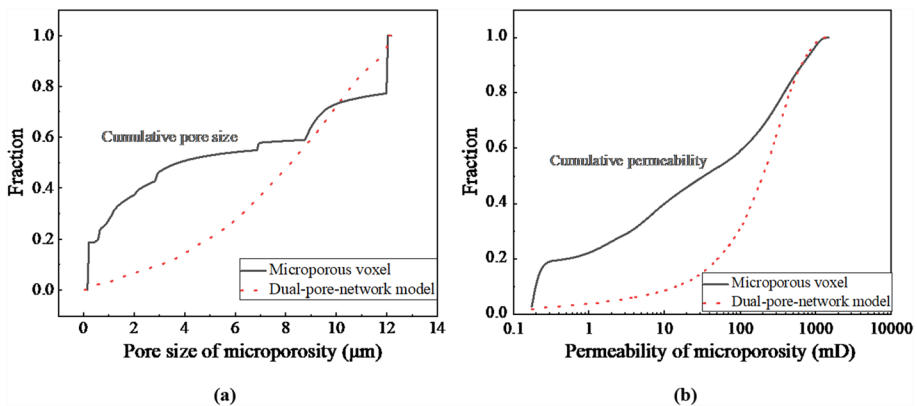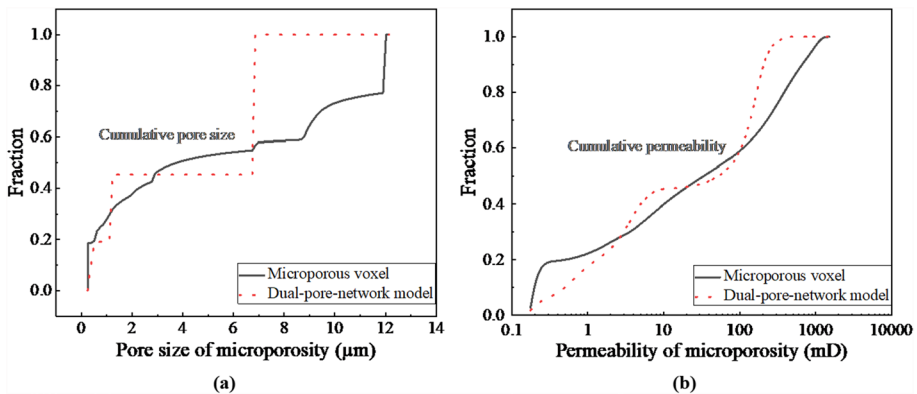

Fig. 8 a Cumulative distributions of the mean pore sizes and **b** the cumulative distributions of the permeability of the original microporosity voxels and the watersheds in the DPNM for ES6.5-2. The mean pore size of each microporosity watershed is calculated by Eq. 13.
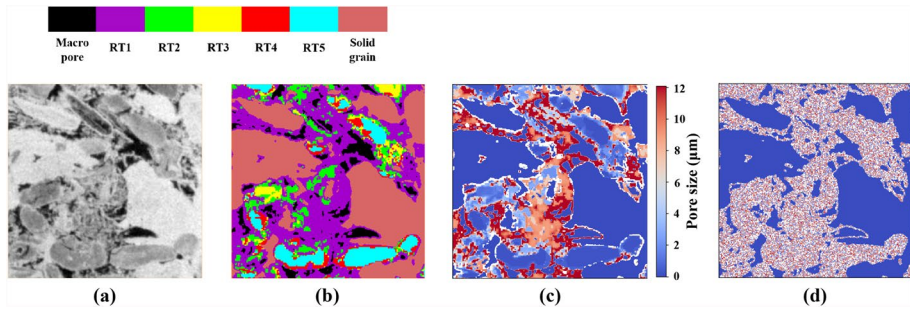
Fig. 9 Schematic of the entry pressure-based sub-rock typing. **a** A 400×400 grayscale slice of ES6.5-2. **b** The five sub-rock types of microporosity, the macropores, and the solid. RT1 to RT5 represent lowest to highest entry capillary pressure microporosity regions. **c** The mean pore size map of microporosity based on the entry capillary pressure. **d** Randomly distributed pore sizes of microporosity.

Fig. 10 **a** Cumulative distributions of the mean pore sizes and **b** the cumulative distributions of the permeability of the original microporosity voxels and the watersheds in the DPNM for ES6.5-2. The entry pressure-based sub-rock typing is used to characterize the mean pore sizes of microporosity.

to estimate the mean pore size of each sub-rock type, and then used the Katz–Thompson model with an assumed tortuosity of 1.75 to estimate the permeability. However, Wang et al. (2022) used a power law, $k = a\varphi^b$, to estimate the permeability where b was set to 3.37 and a was fitted by matching capillary pressure curve.

In multiscale porous media, porosities of microporosity are relatively easy to characterize (Lin et al. 2016, 2017; Ruspini et al. 2016). However, it is costly or even challenging to obtain 3D maps of mean pore sizes in microporosity, which may be prohibitive. An alternatively approach involves using MIP or nuclear magnetic resonance (NMR) T2 spectrum to easily obtain the distribution of mean pore sizes. These mean pore sizes can then be assigned to microporosity voxels. To test this approach, we take the mean pore sizes of ES6.5-2 as the assumed MIP data, which are then randomly assigned to the microporosity for 10 realizations (Fig. 9d). It is found that the predicted average absolute permeability is 45 mD, with a deviation of 10 mD. The underestimation is attributed to the fact that random distributions neglect the correlated distribution of mean pore sizes as clearly shown in Fig. 9b. This indicates that incorporating both the distribution and correlation length of mean pore sizes may enhance the prediction performance.

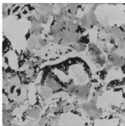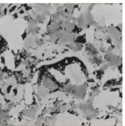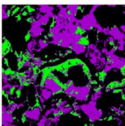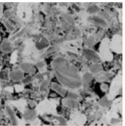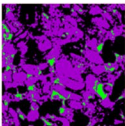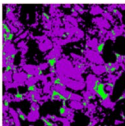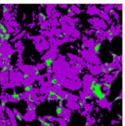## 6.1 Impact of Image Resolution on Permeability
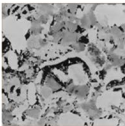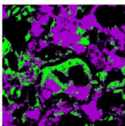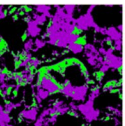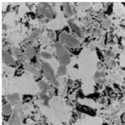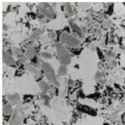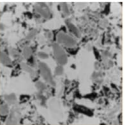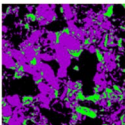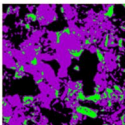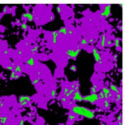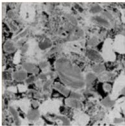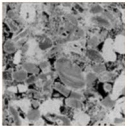
Typically, image resolution and FOV are inversely related. For multiscale digital rock analysis, we hypothesize that reducing image resolution decreases the volume fraction of macropores while increasing the volume fraction of microporosity, leading to underestimation of permeability. To investigate this effect quantitatively, we analyze the three digital rocks of ES3.1, ES3.6, and ES6.5-1 using the DPNM, with the results summarized in Table 7. Leveraging the high computational efficiency of the DPNM, larger domains of the digital rocks are simulated, employing the same microporosity mean pore sizes listed in Table 2. Based on the comparison of permeability predicted by the PNM of macropores (i.e., microporosity is assumed to be impermeable as solid) and by the DPNM, it is seen that ES3.1 has the best connectivity of macropores which contribute to the majority of permeability, whereas ES6.5-1 has the worst connectivity of macropores which are nearly disconnected throughout the flow direction.

The grayscale images are imported into AVIZO, and resampled to produce images with reduced resolutions. This is achieved by halving the resolution (i.e., doubling the original voxel size) and further reducing it by a factor of two (i.e., quadrupling the original voxel size). During the resampling, the grayscale value of each new voxel is calculated as a weighted average of the grayscale values of all original voxels within its corresponding region, using the Lanczos interpolation method (Frangos and Jaimoukha 2008; Jahnavi et al. 2024). For consistency, the same threshold is applied to segment both the original and resampled images, and mean porosities in microporosity are calculated by Eq. 3. Figure 11 shows the schematic of the resampling of the three digital rocks. Direct observations reveal that some small macropores vanish with reduced voxel resolution, and the shapes of macropores become less distinct. In ES6.5-1, the microporosity in purple is far more abundant than the macropores in green. This disparity explains the extremely low permeability of ES6.5-1, which is predominantly governed by microporosity permeability.

Figure 12 illustrates the impact of reducing image resolution on permeability prediction using the DPNM. For each digital rock, the predicted permeability decreases as the image resolution reduces. Meanwhile, it is seen that the volume fraction of macropores decreases, while the volume fraction of microporosity increases. The trend is most pronounced in ES3.6, where the permeability drops significantly from 170 mD at the resolution of 3.6 μm to 14 mD at the resolution of 14.4 μm. In contrast, the changes are less pronounced in ES3.1 and ES6.5-1. It appears that the Lanczos interpolation method plays a crucial role in preserving the boundaries between macropores and microporosity in ES3.1 and ES6.5-1. However, it does not achieve the same effect in ES3.6. Although we have analyzed the distributions of pore sizes of macropores and microporosity, as well as the interfacial areas between macropores and microporosity, identifying the exact cause remains challenging. Upon revisiting the differences among the three digital rocks, we find that the primary distinction lies in their macropore connectivity and volume fractions. ES3.1 has

Table 7 The image sizes and their permeability values of the three digital rocks used in the resolution study

Digital rock	Image size in voxels	By PNM of macropores	By DPNM
ES3.1	1000×1000×1001	271 mD	283 mD
ES3.6	1000×1000×1000	142 mD	170 mD
ES6.5-1	600×600×600	5 nD	8 mD

Sample number	Voxel size (μm)	3.1	6.2	12.4
ES3.1	Original image			
	Segmented image			
	Voxel size (μm)	3.6	7.2	14.4
ES3.6	Original image			
	Segmented image			
	Voxel size (μm)	6.5	13	26
ES6.5-1	Original image			
	Segmented image			

Fig. 11 Schematic of the resampling of the grayscale images of the three digital rocks, namely, ES3.1, ES3.6, and ES6.5-1. In the segmentation, solid, macropores, and microporosity are in black, green, and purple, respectively.

the best connectivity of macropores, which predominantly govern its permeability. ES6.5-1 has the lowest volume fraction of macropores, with microporosity dominating its permeability. ES3.6 lies between the two cases. Based on our preliminary studies, we hypothesize that when macropores are either well connected or poorly connected with abundant microporosity, the impact of image resolution is minimal. This provides a useful guideline for balancing the FOV and image resolution. Finally, further studies are needed, utilizing

Fig. 12 The impact of image resolution on the permeability (predicted by the DPNM) and the volume fractions of segmented macropores and microporosity for the three digital rocks, namely, ES3.1, ES3.6, and ES6.5-1.
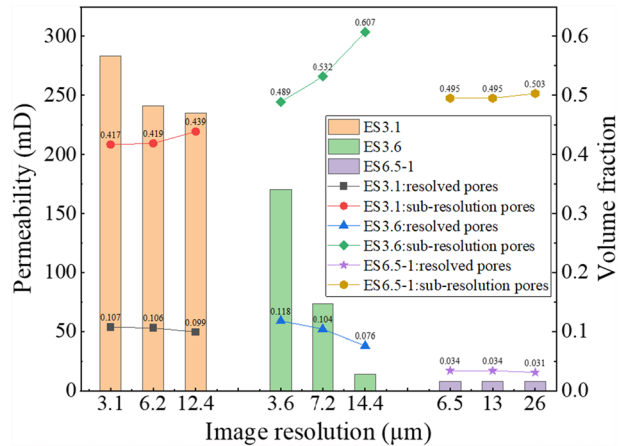
clustering and correlation analysis of various image features and parameters, to gain a deeper understanding of how image resolution influences the predicted permeability.

7 Conclusions and Outlook

Three types of hybrid pore-scale models have been proposed in the literature to address flow and transport in multiscale porous media, including micro-continuum models (MCMs), dual-pore-network models (DPNMs), and pore-network-continuum models (PNCMs). Among these, MCMs are the most accurate but also the most computational demands. DPNMs are the most computationally efficient and have the potential for core-scale modeling, although they may introduce significant numerical errors. PNCMs are designed to balance both accuracy and efficiency. In this work, we have developed an image-based DPNM and an image-based PNCM to predict absolute permeability and formation factor. Several publicly available digital rocks with both homogeneous and heterogeneous microporosity are selected as test multiscale porous media. With the help of a reference model verified against MCMs, we perform comprehensive comparisons between the DPNM and PNCM, focusing on the strengths and limitations of the DPNM. Additionally, we study the impact of image resolution on permeability prediction by the DPNM. Based on our case studies, the following main conclusions are drawn:

1. Both the DPNM and PNCM can well predict absolute permeability and formation factors of multiscale digital rocks with microporosity of uniform mean pore sizes and heterogeneous porosities. In this context, the DPNM proves superior to the PNCM due to its computational efficiency.
2. For multiscale digital rocks with microporosity of heterogeneous mean pore sizes and porosities, the PNCM remains accurate in predicting absolute permeability. In contrast, the DPNM significantly underestimates absolute permeability by more than an order of magnitude. The poor performance stems from the upscaled mean pore sizes of microporosity watersheds, which substantially underestimate the actual mean pore sizes within microporosity. To enhance the predictive accuracy of the DPNM, two methods have

been tested including the arithmetic averaging of mean pore sizes within a microporosity watershed and the entry pressure-based sub-rock typing. Both methods significantly improve the performance.

3. An appropriate interpolation method for downsampling multiscale digital rocks can effectively preserve the boundaries between macropores and microporosity. When macropores are either well-connected or poorly connected with abundant microporosity, the effect of image resolution on permeability prediction is minimal.

We have demonstrated that both DPNMs and PNCMs hold great potential for quantitatively predicting single-phase flow. Future research should focus on validating two-phase flow predictions, such as capillary pressure and relative permeability, as well as transient flow and transport processes. Addressing these challenges will broaden their applicability to a wider range of geological and engineering systems.

Appendix 1

Estimation of Uniform Mean Pore Sizes in Microporosity

For a multiscale porous medium, instead of experimental characterization of mean pore sizes in microporosity, we can estimate uniform mean pores sizes by the MIP curve (Bultreys et al. 2015). The procedure is as follows. Firstly, for a given MIP curve, after converting capillary pressure to pore radius by the Young-Laplace equation, we obtain the curve of mercury saturation with respect to pore radius as shown in Fig. 13. Then, we assume that pores with an inscribed radius smaller than the voxel size (i.e., image resolution) belong to microporosity. In this work, as shown in Fig. 13, 3.1 μm, 3.6 μm and 6.5 μm correspond to the mercury saturation of S_1, S_2, and S_3, respectively. S_0 represents an upper limit of 0.98. Finally, uniform mean pore sizes are calculated as (Zhang et al. 2023):

$$r_n = \frac{\int_{S_0}^{S_n} R(s)\mathrm{d}s}{S_0 - S_n}, \ n = 1, 2, 3 \tag{14}$$

where r_n is the mean pore size of microporosity, and $R(s)$ is given by the curve of mercury saturation with respect to pore radius.

Author Contributions Xingyuan Zhao contributed to writing—original draft preparation. Xingyuan Zhao, Bowen Shi, Xin Wang, Jianlin Zhao, Fei Jiang contributed to methodology, simulation, analysis. Chao-Zhong Qin contributed to supervision, review and editing.

Data Availability All data in this paper will be available upon request at chaozhong.qin@gmail.com.

Fig. 13 Relationship between mercury saturation and pore radius from the MIP test
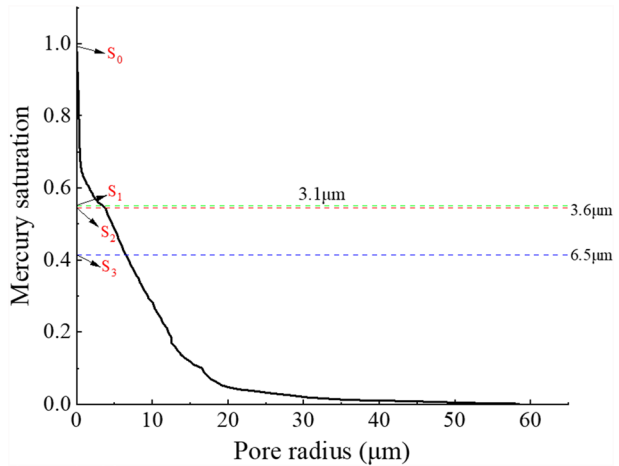
Declarations

Competing interest The authors have no competing interests to declare that are relevant to the content of this article.

References

Alyafei, N., Blunt, M.J.: The effect of wettability on capillary trapping in carbonates. Adv. Water Resour. **90**, 36–50 (2016). https://doi.org/10.1016/j.advwatres.2016.02.001

Bauer, D., Youssef, S., Fleury, M., Bekri, S., Rosenberg, E., Vizika, O.: Improving the estimations of petrophysical transport behavior of carbonate rocks using a dual pore network approach combined with computed microtomography. Transp. Porous Med. **94**(2), 505–524 (2012). https://doi.org/10.1007/s11242-012-9941-z

Blunt, M.J., Bijeljic, B., Dong, H., Gharbi, O., Iglauer, S., Mostaghimi, P., Paluszny, A., Pentland, C.: Pore-scale imaging and modelling. Adv. Water Resour. **51**, 197–216 (2013). https://doi.org/10.1016/j.advwatres.2012.03.003

Bultreys, T., Stappen, J.V., Kock, T.D., Boever, W.D., Boone, M.A., Hoorebeke, L.V., Cnudde, V.: Investigating the relative permeability behavior of microporosity-rich carbonates and tight sandstones with multiscale pore network models. J. Geophys. Res. Solid Earth **121**, 7929–7945 (2016). https://doi.org/10.1002/2016JB013328

Bultreys, T., Van Hoorebeke, L., Cnudde, V.: Multi-scale, micro-computed tomography-based pore network models to simulate drainage in heterogeneous rocks. Adv. Water Resour. **78**, 36–49 (2015). https://doi.org/10.1016/j.advwatres.2015.02.003

Carrillo, F.J., Bourg, I.C.: A Darcy–Brinkman-biot approach to modeling the hydrology and mechanics of porous media containing macropores and deformable microporous regions. Water Resour. Res. **55**(7), 8096–8121 (2019). https://doi.org/10.1029/2019WR024712

Carrillo, F.J., Bourg, I.C., Soulaine, C.: Multiphase flow modeling in multiscale porous media: an open-source micro-continuum approach. J. Comput. Phys. **X**(8), 100073 (2020). https://doi.org/10.1016/j.jcpx.2020.100073

Dong, H., Blunt, M.J.: Pore-network extraction from micro-computerized-tomography images. Phys. Rev. E **80**, 036307 (2009). https://doi.org/10.1103/PhysRevE.80.036307

El-Dieb, A.S., Hooton, R.D.: Evaluation of the Katz-Thompson model for estimating the water permeability of cement-based materials from mercury intrusion porosimetry data. Cement Concrete Res. **24**(3), 443–455 (1994). https://doi.org/10.1016/0008-8846(94)90131-7

Foroughi, S., Bijeljic, B., Gao, Y., Blunt, M.J.: Incorporation of Sub-resolution porosity into two-phase flow models with a multiscale pore network for complex microporous rocks. Water Resour. Res. **60**(5), e2023WR036393 (2024). https://doi.org/10.1029/2023WR036393

Frangos, M., Jaimoukha, I.M.: Adaptive rational interpolation: Arnoldi and Lanczos-like equations. Eur. J. Control. **14**, 342–354 (2008). https://doi.org/10.3166/ejc.14.342-354

Fu, J., Thomas, H.R., Li, C.: Tortuosity of porous media: image analysis and physical simulation. Earth-Sci. Rev. **212**, 103439 (2021). https://doi.org/10.1016/j.earscirev.2020.103439

Gershenzon, N.I., Ritzi, R.W., Jr., Dominic, D.F., Mehnert, E., Okwen, R.T.: Comparison of CO2 trapping in highly heterogeneous reservoirs with Brooks–Corey and van Genuchten type capillary pressure curves. Adv. Water Resour. **96**, 225–236 (2016). https://doi.org/10.1016/j.advwatres.2016.07.022

Gostick, J.T.: Versatile and efficient pore network extraction method using marker-based watershed segmentation. Phys. Rev. E **96**(2–1), 023307 (2017). https://doi.org/10.1103/PhysRevE.96.023307

Guo, B., Ma, L., Tchelepi, H.A.: Image-based micro-continuum model for gas flow in organic-rich shale rock. Adv. Water Resour. **122**, 70–84 (2018). https://doi.org/10.1016/j.advwatres.2018.10.004

Guo, Z., Zhao, T.S.: Lattice Boltzmann model for incompressible flows through porous media. Phys. Rev. E **66**(3), 036304 (2002). https://doi.org/10.1103/PhysRevE.66.036304

Hakimov, N., Syed, F.I., Muther, T., Dahaghi, A.K., Negahban, S.: Pore-scale network modeling approach to study the impact of Microporosity's pore space topology. Microporous Mesoporous Mater. **338**(15), 111918 (2022). https://doi.org/10.1016/j.micromeso.2022.111918

Heinemann, N., Alcalde, J., Miocic, J.M., Hangx, S.J.T., Kallmeyer, J., Ostertag-Henning, C., Hassanpouryouzband, A., Thaysen, E.M., Strobel, G.J., Schmidt-Hattenberger, C., Edlmann, K., Wilkinson, M., Bentham, M., Stuart Haszeldine, R., Carbonell, R., Rudloff, A.: Enabling large-scale hydrogen storage in porous media—the scientific challenges. Energy Environ. Sci. **14**(2), 853–864 (2021). https://doi.org/10.1039/D0EE03536J

Jahnavi, M., Rao, D.R., Sujatha, A.: A comparative study of super-resolution interpolation techniques: insights for selecting the most appropriate method. Procedia Comput. Sci. **233**, 504–517 (2024). https://doi.org/10.1016/j.procs.2024.03.240

Jalilinasrabady, S., Tanaka, T., Itoi, R., Goto, H.: Numerical simulation and production prediction assessment of Takigami geothermal reservoir. Energy **236**, 121503 (2021). https://doi.org/10.1016/j.energy.2021.121503

Jiang, Z., van Dijke, M.I.J., Sorbie, K.S., Couples, G.D.: Representation of multiscale heterogeneity via multiscale pore networks: representation of multiscale heterogeneity. Water Resour. Res. **49**(9), 5437–5449 (2013). https://doi.org/10.1002/wrcr.20304

Khan, Z.A., Gostick, J.T.: Enhancing pore network extraction performance via seed-based pore region growing segmentation. Adv. Water Resour. **183**(1), 104591 (2024). https://doi.org/10.1016/j.advwatres.2023.104591

Khan, Z.A., Tranter, T., Agnaou, M., Elkamel, A., Gostick, J.: Dual network extraction algorithm to investigate multiple transport processes in porous materials: Image-based modeling of pore and grain scale processes. Comput. Chem. Eng. **123**, 64–77 (2019). https://doi.org/10.1016/j.compchemeng.2018.12.025

Koch, T., Weishaupt, K., Müller, J., Weigand, B., Helmig, R.: A (dual) network model for heat transfer in porous media: toward efficient model concepts for coupled systems from fuel cells to heat exchangers. Transp. Porous Med. **140**(1), 107–141 (2021). https://doi.org/10.1007/s11242-021-01602-5

Li, W., Cao, J., Liang, Y., Masuda, Y., Tsuji, T., Tamura, K., Ishiwata, T., Kuramoto, D., Matsuoka, T.: Evaluation of CO2 storage and enhanced gas recovery potential in gas shale using kerogen nanopore systems with mesopores and micropores. Chem. Eng. J. **486**, 150225 (2024). https://doi.org/10.1016/j.cej.2024.150225

Lin, Q., Al-Khulaifi, Y., Blunt, M.J., Bijeljic, B.: Quantification of sub-resolution porosity in carbonate rocks by applying high-salinity contrast brine using X-ray microtomography differential imaging. Adv. Water Resour. **96**, 306–322 (2016). https://doi.org/10.1016/j.advwatres.2016.08.002

Lin, Q., Bijeljic, B., Rieke, H., Blunt, M.J.: Visualization and quantification of capillary drainage in the pore space of laminated sandstone by a porous plate method using differential imaging X-ray microtomography. Water Resour. Res. **53**(7), 7457–7468 (2017). https://doi.org/10.1002/2017WR021083

Ling, K., Han, G., Shen, Z., Ghalambor, A., He, J., Pei, P.: Calculating pore size distribution by using capillary pressure. In: Day 2 Thu, February 27, 2014. Presented at the SPE International Symposium and Exhibition on Formation Damage Control, SPE, Lafayette, Louisiana, p. D021S008R005 (2014). https://doi.org/10.2118/168183-MS

Liu, J., ZhangSun, T.T.S.: A new pixel-free algorithm of pore-network extraction for fluid flow in porous media: flashlight search medial axis. Adv. Geo-Energy Res. **13**, 32–41 (2024). https://doi.org/10.46690/ager.2024.07.05

Mehmani, A., Prodanović, M.: The effect of microporosity on transport properties in porous media. Adv. Water Resour. **63**, 104–119 (2014). https://doi.org/10.1016/j.advwatres.2013.10.009

Mehmani, A., Prodanović, M., Javadpour, F.: Multiscale, multiphysics network modeling of shale matrix gas flows. Transp. Porous Med. **99**, 377–390 (2013). https://doi.org/10.1007/s11242-013-0191-5

Menke, H.P., Gao, Y., Linden, S., Andrew, M.G.: Using nano-XRM and high-contrast imaging to inform micro-porosity permeability during stokes-brinkman single and two-phase flow simulations on micro-CT images. Front. Water **4**(34), 935035 (2022). https://doi.org/10.3389/frwa.2022.935035

Moslemipour, A., Sadeghnejad, S.: Dual-scale pore network reconstruction of vugular carbonates using multi-scale imaging techniques. Adv. Water Resour. **147**, 103795 (2021). https://doi.org/10.1016/j.advwatres.2020.103795

Pinder, G.F., Gray, W.G.: Essentials of Multiphase Flow and Transport in Porous Media: Pinder/Multiphase Flow. Wiley, Hoboken (2008)

Rabbani, A., Babaei, M., Javadpour, F.: A triple pore network model (T-PNM) for gas flow simulation in fractured, micro-porous and meso-porous media. Transp. Porous Med. **132**(4), 707–740 (2020). https://doi.org/10.1007/s11242-020-01409-w

Ruspini, L.C., Lindkvist, G., Bakke, S.., Alberts, L.., Carnerup, A.M., Øren, P.E.: A multi-scale imaging and modeling workflow for tight rocks. In: All Days. Presented at the SPE Low Perm Symposium, SPE, Denver, Colorado, p. SPE-180268-MS (2016). https://doi.org/10.2118/180268-MS

Ruspini, L.C., Øren, P.E., Berg, S., Masalmeh, S., Bultreys, T., Taberner, C., Sorop, T., Marcelis, F., Appel, M., Freeman, J., Wilson, O.B.: Multiscale digital rock analysis for complex rocks. Transp. Porous Med. **139**, 301–325 (2021). https://doi.org/10.1007/s11242-021-01667-2

Shi, B., Jiang, H., Guo, B., Tian, J., Qin, C.-Z.: Modeling of flow and transport in multiscale digital rocks aided by grid coarsening of microporous domains. J. Hydrol. **633**, 131003 (2024). https://doi.org/10.1016/j.jhydrol.2024.131003

Soulaine, C.: Micro-continuum modeling: an hybrid-scale approach for solving coupled processes in porous media. Water Resour. Res. **60**, e2023WR035908 (2024). https://doi.org/10.1029/2023WR035908

Spurin, C., Bultreys, T., Bijeljic, B., Blunt, M.J., Krevor, S.: Intermittent fluid connectivity during two-phase flow in a heterogeneous carbonate rock. Phys. Rev. E **100**(4), 043103 (2019a). https://doi.org/10.1103/PhysRevE.100.043103

Spurin, C., Bultreys, T., Bijeljic, B., Blunt, M.J., Krevor, S.: Mechanisms controlling fluid breakup and reconnection during two-phase flow in porous media. Phys. Rev. E **100**(4–1), 043115 (2019b). https://doi.org/10.1103/PhysRevE.100.043115

Tang, Y.B., Li, M., Bernabé, Y., Tang, H.M., Li, X.F., Bai, X.Y., Tao, Z.W.: A new electrical formation factor model for bimodal carbonates: numerical studies using dual-pore percolation network. Geophys. J. Int. **201**(3), 1456–1470 (2015). https://doi.org/10.1093/gji/ggv073

Tanino, Y., Blunt, M.J.: Capillary trapping in sandstones and carbonates: dependence on pore structure. Water Resour. Res. **48**(8), 2011WR011712 (2012). https://doi.org/10.1029/2011WR011712

Tiab, D., Donaldson, E.C.: Petrophysics: Theory and Practice of Measuring Reservoir Rock and Fluid Transport Properties. Elsevier, Amsterdam (2016)

Tjaden, B., Finegan, D.P., Lane, J., Brett, D.J.L., Shearing, P.R.: Contradictory concepts in tortuosity determination in porous media in electrochemical devices. Chem. Eng. Sci. **166**, 235–245 (2017). https://doi.org/10.1016/j.ces.2017.03.051

Wang, S., Ruspini, L.C., Øren, P., Van Offenwert, S., Bultreys, T.: Anchoring multi-scale models to micron-scale imaging of multiphase flow in rocks. Water Resour. Res. (2022). https://doi.org/10.1029/2021WR030870

Zhang, G., Foroughi, S., Raeini, A.Q., Blunt, M.J., Bijeljic, B.: The impact of bimodal pore size distribution and wettability on relative permeability and capillary pressure in a microporous limestone with uncertainty quantification. Adv. Water Resour. **171**, 104352 (2023). https://doi.org/10.1016/j.advwatres.2022.104352

Zhang, L.: A hybrid pore-network-continuum modeling framework for flow and transport in 3D digital images of porous media. Adv. Water Resour. **128**(8), 104753 (2024). https://doi.org/10.1016/j.advwatres.2024.104753

Zhao, J., Liu, Y., Qin, F., Fei, L.: Pore-scale fluid flow simulation coupling lattice Boltzmann method and pore network model. Capillarity **7**, 41–46 (2023). https://doi.org/10.46690/capi.2023.06.01

Zhao, J., Qin, F., Derome, D., Carmeliet, J.: Simulation of quasi-static drainage displacement in porous media on pore-scale: coupling lattice Boltzmann method and pore network model. J. Hydrol. **588**, 125080 (2020). https://doi.org/10.1016/j.jhydrol.2020.125080

Zhao, J., Yao, J., Zhang, L., Sui, H., Zhang, M.: Pore-scale simulation of shale gas production considering the adsorption effect. Int. J. Heat Mass Transf. **103**(1), 1098–1107 (2016). https://doi.org/10.1016/j.ijheatmasstransfer.2016.08.026